First-Principles Investigations of the Structural, Anisotropic Mechanical, Thermodynamic and Electronic Properties of the AlNi$_2$Ti Compound

Shuli Tang, Yefei Li *, Yimin Gao, Qiaoling Zheng, Zhiwei Liu and Xiangyi Ren

State Key Laboratory for Mechanical Behavior of Materials, Xi'an Jiaotong University, Xi'an 710049, China; shulitangxjtu@126.com (S.T.); ymgao@mail.xjtu.edu.cn (Y.G.); qlzxjtu@163.com (Q.Z.); yhcheng_36@163.com (Z.L.); mmerenxiangyi@126.com (X.R.)

* Correspondence: yefeili@126.com; Tel.: +86-29-8266-5479

Abstract: In this paper, the electronic, mechanical and thermodynamic properties of AlNi$_2$Ti are studied by first-principles calculations in order to reveal the influence of AlNi$_2$Ti as an interfacial phase on ZTA (zirconia toughened alumina)/Fe. The results show that AlNi$_2$Ti has relatively high mechanical properties, which will benefit the impact or wear resistance of the ZTA/Fe composite. The values of bulk, shear and Young's modulus are 164.2, 63.2 and 168.1 GPa respectively, and the hardness of AlNi$_2$Ti (4.4 GPa) is comparable to common ferrous materials. The intrinsic ductile nature and strong metallic bonding character of AlNi$_2$Ti are confirmed by B/G and Poisson's ratio. AlNi$_2$Ti shows isotropy bulk modulus and anisotropic elasticity in different crystallographic directions. At room temperature, the linear thermal expansion coefficient (LTEC) of AlNi$_2$Ti estimated by quasi-harmonic approximation (QHA) based on Debye model is 10.6×10^{-6} K^{-1}, close to LTECs of zirconia toughened alumina and iron. Therefore, the thermal matching of ZTA/Fe composite with AlNi$_2$Ti interfacial phase can be improved. Other thermodynamic properties including Debye temperature, sound velocity, thermal conductivity and heat capacity, as well as electronic properties, are also calculated.

Keywords: first-principles calculation; mechanical modulus; anisotropy; thermal expansion coefficient; specific heat capacity

1. Introduction

AlNi$_2$Ti is one of the Heusler compounds first identified by Heusler in 1903 [1]. The Heusler compounds are a group of ternary intermetallic alloys formed at the stoichiometric composition X$_2$YZ (generally, X and Y are transition metals and Z is a b-subgroup element), with the doubly ordered $L2_1$ structure based on the ordered B2 [2]. They have been widely reported to have excellent ferromagnetic, paramagnetic, mechanical and thermoelectric properties [3,4]. AlNi$_2$Ti with $L2_1$ structure can provide NiAl or Ni-base and Ti-base alloys with good high-temperature mechanical properties by precipitate strengthening [5–16]. Especially the mechanical properties of Fe-Ni-Al-Ti ferritic alloys, such as creep resistance and yield strength, can be significantly enhanced due to the AlNi$_2$Ti precipitates [17–26]. In addition, AlNi$_2$Ti precipitate phase has also been observed in microstructures of Al-doped Ni-Ti shape memory alloys that have huge potential to be applied as functional material in many areas such as clinical medicine, biotechnology, automation, energy engineering, electronics industry, aeronautics and astronautics, owing to their pseudoelasticity, superplasticity and shape memory properties [27–32].

AlNi$_2$Ti is also a common reaction product at the interface between phases. Recently, AlNi$_2$Ti was observed at the interface in zirconia-toughened alumina (ZTA) or Al$_2$O$_3$ reinforced iron matrix composite with an Ni-Ti transition layer that is expected to be applied for wear-resistant material [33,34].

The active elements Ni and Ti can promote the atom diffusion and chemical reaction between ZTA and Fe. Thus, Al_2O_3 will decompose and diffuse into the Ni-Ti layer, leading to the formation of interfacial phase $AlNi_2Ti$. The mechanical and thermal performance of $AlNi_2Ti$ is a key point for improving the interface properties and then wear resistance of composites, especially the thermal expansion coefficient (TEC) that influences the thermal matching of composite interfaces.

By now, a number of research works have been carried out on $AlNi_2Ti$ and other Heusler compounds by first-principles calculations. Wen et al. [35] reported the elastic constants and mechanical moduli under different pressures or temperatures of Ni_2XAl (X = Sc, Ti, V) compounds. The thermodynamic properties including heat capacity and thermal expansion coefficient as a function of temperature and pressure were demonstrated. They claimed that the influence of pressure on moduli and hardness decreases as the sequence of Ni_2ScAl > Ni_2TiAl > Ni_2VAl, while it has an opposite effect on ductility or anisotropy. Reddy and Kanchana [36] studied the effect of pressure and temperature on the Fermi surface and dynamic properties of a series of compounds Ni_2XAl (X = Ti, V, Zr, Nb, Hf and Ta) using density functional theory (DFT). Their calculating results suggested that $AlNi_2Ti$ has lower specific heat and entropy but higher internal energy and free energy among the considered compounds [36]. The superconducting property of Ni_2NbAl has also been studied and the critical superconducting transition temperature Tc calculated to be 3.1 K [36], which agrees well with the experimental result (Tc around 2.1 K) in previous work [37]. Compared with representative high-pressure superconductors, such as H_3S (Tc: 178 K), PH_3 (Tc: 81 K) [38] and PtH (Tc: 12.94~20.01 K) [39], Ni_2NbAl performs at a relatively low value of Tc. Sahariya and Ahuja [40] presented the energy bands and density of states of $AlNi_2Ti$ calculated using the DFT by linear combination of atomic orbitals (LCAO) approach. Zhou et al. [41] investigated the electronic and magnetic properties of $AlNi_2Ti$ affected by swap defects and atomic antisite using first-principles calculations. The $Ni_{Ti(A)}$ antisite was found to be the most probable defect because of the lowest formation energy. Nevertheless, the properties of $AlNi_2Ti$ are still short of systematic theoretical study, especially the thermal properties and their anisotropies.

In this paper, a comprehensive and complementary study of the mechanical and thermal properties of $AlNi_2Ti$ crystal is conducted by first-principles calculation in order to provide significant theoretical directions for the fabrication and application of composites with interfacial phase $AlNi_2Ti$ and to offer a reference for the future research into $AlNi_2Ti$ or other Heusler alloys.

2. Calculation Methods

The $L2_1$ cubic crystal structure with the $Fm\bar{3}m$ space group of $AlNi_2Ti$ is shown in Figure 1. The unit cell of $AlNi_2Ti$ has four formulas with a total of 16 atoms.
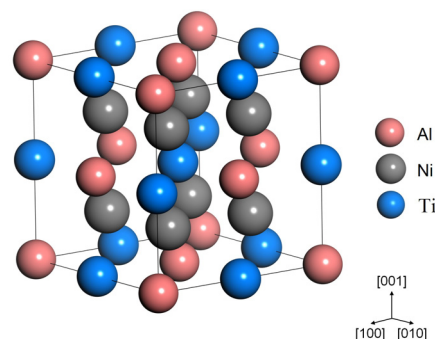
Figure 1. Crystal structure calculated for $AlNi_2Ti$ compounds.

The first-principles calculations based on DFT were implemented in Cambridge Serial Total Energy Package (CASTEP) code [42–44]. The ultra-soft pseudo potentials were employed to represent the interactions between ionic core and valence electrons. The valence electron configurations for

Al, Ni and Ti were $3s^2\,3p^1$, $3d^8\,4s^2$ and $3s^2\,3p^6\,3d^2\,4s^2$, respectively. A special *k*-point mesh was used for the numerical integrations in the entire Brillouin zone by setting as $8 \times 8 \times 8$ grid [45]. The Broyden–Fletcher–Goldfarb–Shannon (BFGS) minimization scheme was utilized for the optimization of lattice parameters and atomic positions in order to obtain the ground-state crystal structure. For the purpose of providing more abundant and reliable results, two approaches, i.e., the generalized gradient approximation (GGA) of Perdew Burke Ernzerhof (PBE) and Perdew Wang in 1991 (PW91) approaches, were adopted in exchange–correlation energy calculations [46]. It is capable of comparison with other DFT studies on $AlNi_2Ti$ by the same PBE-GGA approach [35,36] and local density approximation (LDA) approach [7,35]. A kinetic energy cut-off value of 500 eV was used for plane wave expansions. The self-consistence convergence of the energy was set to 0.5×10^{-6} eV/atom. The quasi-harmonic approximation (QHA) Debye model was applied to predict the thermal properties of $AlNi_2Ti$ compounds.

3. Results and Discussion

3.1. Crystal Parameters and Mechanical Properties

The optimized ground-state structural parameters of $AlNi_2Ti$ compounds calculated by the GGA-PBE and GGA-PW91 approaches are shown in Table 1. It can be seen that the lattice parameters at 0 K in this study are close to other theoretical and experimental data [22,35,36,47–54]. The average deviation of results in this work to references for lattice parameters is less than 1%. The chemical stability of the $AlNi_2Ti$ compound was evaluated by the cohesive energy E_{coh} and formation enthalpy $\Delta_r H$, which can be calculated using equations as follows [55].

$$E_{coh}(AlNi_2Ti) = E_{tot}(AlNi_2Ti) - E_{iso}(Al) - 2E_{iso}(Ni) - E_{iso}(Ti) \tag{1}$$

$$\Delta_r H(AlNi_2Ti) = E_{coh}(AlNi_2Ti) - E_{coh}(Al) - 2E_{coh}(Ni) - E_{coh}(Ti) \tag{2}$$

where E_{tot} represents the total energy of material and E_{iso} represents the total energy of a single atom. From the calculated result in Table 1, the negative values of formation enthalpy and cohesive energy indicate the thermodynamic stability of $AlNi_2Ti$.

Table 1. The optimized ground-state structural parameters (*a*, *b*, *c*, in Å; V_{cell} in Å^3; ρ in g/cm^3), atomic site, cohesive energy (E_{coh}, eV/f.u.) and formation enthalpy ($\Delta_r H$, eV/atom) of $AlNi_2Ti$ intermetallic compound.

Method	Lattice Parameters $a = b = c$	V_{cell}	ρ	Al	Ni	Ti	$\Delta_r H$	E_{coh}
GGA-PBE	5.908 (5.865 [a])	206.242 (201.75 [a])	6.193 (6.33 [a])	4a (0, 0, 0)	8c (0.25, 0.25, 0.25)	4b (0.5, 0.5, 0.5)	−0.671	−27.602
GGA-PW91	5.903	205.676	6.210				−0.643	−33.173
Other cal. data	5.906 [b], 5.90 [c], 5.828 [d]						−0.658 [b], −0.662 [m]	
Exp. data	5.906 [e], 5.883–5.910 [f], 5.819 [g], 5.876 [i], 5.942 [j], 5.889 [k], 5.865–5.886 [l]	203.61–206.40 [f]					−0.747 [e], −0.578 [h], −0.579 [n]	
EOS	5.911	206.499	6.186					

[a] From Inorganic Crystal Structure Database (ICSD) #58063; [b] Calculation data evaluated by GGA in [35]; [c] Cal. data evaluated by Reddy, et al. in [36]; [d] Cal. data evaluated by Monte Carlo simulations in [11]; [e] Exp. data in [47]; [f] Exp. data from [48]; [g] Data calculated from the selected area electron diffraction pattern in [22]; [h] Exp. data from [49]; [i] Data from handbook [50]; [j] Exp. data measured by X-ray diffraction in [51]; [k] Exp. data in [52]; [l] Exp. data in [53]; [m] Calculated values from a thermodynamic database in [54]; [n] Data measured by high-temperature reaction calorimeter in [54].

In order to study the mechanical properties of $AlNi_2Ti$ under external stress, the second-order elastic constants c_{ij} are calculated by stress versus strain without stress controls. The stress–strain method is conducted using strain modes $[\varepsilon]^T = \eta[1\,0\,0\,1\,0\,0]$, where $[\varepsilon]^T$ is the transpose of the strain

matrix with Voigt notation and η is the magnitude of strain [56]. The maximum strain amplitude is set as 0.003 and the number of steps for each strain is four. Then elastic constants c_{ij} can be computed by Hooker's law, as presented in Table 2. Our results are similar to other calculation data [18,35,36] and the values from the GGA-PW91 method are quite close to those from GGA-PBE. All elastic constants satisfy the Born–Huang stability criterion, so the AlNi$_2$Ti compound has intrinsic stability [57]. The detailed criterion for cubic structure is that an elastically stable crystal should follow restrictions: $c_{44} > 0$, $c_{11} > c_{12}$, and $c_{11} + 2c_{12} > 0$ [58–60]. The value of c_{11} is much larger than c_{12} and c_{44}, indicating that it is stiff against uniaxial strain ε_1. Then the bulk modulus (B) and shear modulus (G) are computed by Voigt–Reuss–Hill approximation [61]. The Young's modulus E, Poisson's ratio v and Vicker's hardness Hv are estimated by well-known relations $E = 9BG/(3B + G)$, $v = (3B − 2G)/(6B + 2G)$ [62–65] and $Hv = 2(k^2G)^{0.585} − 3$, where $k = G/B$ [66]. The results show that the hardness of AlNi$_2$Ti (4.4 GPa) is comparable to some common ferrous materials like pearlite steel (about 2 GPa), martensite steel (about 5.5 GPa) and white cast iron (about 6 GPa). Compared with Ni-Ti binary compounds, the hardness of AlNi$_2$Ti is much higher than NiTi (2.7 or 1.1 GPa with B2 or B19' structure respectively) and NiTi$_2$ (1.6 GPa), and the mechanical moduli of AlNi$_2$Ti are also higher than NiTi and NiTi$_2$, but lower than Ni$_3$Ti [55]. The Poisson's ratio of AlNi$_2$Ti is determined as 0.32. Since the Poisson's ratio is normally 0.25 for covalent materials and 0.3 for metallic materials, our result indicates that AlNi$_2$Ti has a strong metallic bonding character. Besides, the value of B/G is a criterion for justifying the ductility of the material; for tough materials, $B/G > 1.75$, and for brittle materials, $B/G < 1.75$. The B/G value (2.6) indicates that AlNi$_2$Ti has relatively higher toughness and ductility than common ceramics, such as WC ($B/G = 1.37$ [67]), SiO$_2$ (1.39 [68]), TiC (1.41 [69,70]), Al$_2$O$_3$ (1.52 [71]) and ZrO$_2$ (2.3 [71]). Therefore, the existence of AlNi$_2$Ti at the ZTA/Fe interface will benefit the mechanical properties of the composite with considerable certainty. Our results are close to other calculated data, except for hardness, which was estimated by another empirical equation in reference [35].

Table 2. Calculated independent elastic constants (GPa) compared to experimental and other theoretical values for the single crystalline AlNi$_2$Ti intermetallic compound. Hereafter the mechanical modulus (GPa), Poisson's ratio, Vicker's hardness, shear anisotropic factors, and percent anisotropic index are also provided.

Method	Elastic Constants			B			G			B_H/G_H	E	v	H_V	Shear Anisotropic Factors				Anisotropic Index	
	c_{11}	c_{12}	c_{44}	B_V	B_R	B_H	G_V	G_R	G_H					A_1	A_2	A_3	A_B	A_G	A^U
GGA-PBE	208.1	142.2	97.6	164.2	164.2	164.2	71.8	54.7	63.2	2.6	168.1	0.32	4.4	2.96	2.96	2.96	0.00	0.14	1.56
GGA-PW91	209.3	143.4	94.8	165.4	165.4	165.4	70.1	54.2	62.1	2.7	165.6	0.33	4.1	2.88	2.88	2.88	0.00	0.13	1.47
Cal. data [a]	215.8 [a], 223 [b]	139.4 [a], 135 [b]	98.7 [a], 104 [b]		164.9 [a], 164 [b]			67.5 [a], 74 [b]		2.4 [a]	178.1 [a], 193 [b]		8.1 [a]		2.36 [b]			0.104 [a]	1.165 [a]
Exp. data	120 [c]	97 [c]	56 [c]																
EOS					162.9														

[a] Cal. data from [35]; [b] Cal. data from [36]; [c] Data adjusted by comparing with experimental diffraction elastic constants in [18];

The Helmholtz free energy is calculated by the following equation to investigate the stability of AlNi$_2$Ti under elevated temperature [45]:

$$E(V, T) = E_{gs}(V) + E_{vib}(V, T) + E_{ele}(V, T), \tag{3}$$

where E_{gs} refers to the ground state total energy; E_{vib} refers to vibrational free energy which can be given by QHA approximation based on the Debye model; E_{ele} refers to the electron thermal excitations at finite temperature. Then the equilibrium volume and bulk modulus at the certain temperature can be obtained from isothermal curves ($E(V, T)$-V) by fitting the Birch–Murnaghan equation of state as follows [72–74]:

$$E(V) = \frac{B_0 V_0}{B_0'} \left[\frac{1}{B_0' - 1} \left(\frac{V}{V_0} \right)^{(1-B_0')} + \frac{V}{V_0} + \frac{B_0'}{1 - B_0'} \right] + E_0, \tag{4}$$

Here $E(V)$ represents the Helmholtz free energy of crystal with a volume of V; E_0, B_0 and V_0 are the energy, bulk modulus and cell volume, respectively, under 0 K; B'_0 refers to the first-order derivative of bulk modulus versus pressure under 0 K. Then the computed lattice parameters and bulk moduli as the function of temperature are shown in Figure 2. It can be seen that with the rise of temperature from 0 to 1500 K, the lattice parameter increases from 5.91 to 6.01 Å while the bulk modulus declines from 162.95 to 138.05 GPa. The result indicates that $AlNi_2Ti$ is not particularly stable under elevated temperatures and there might be a certain amount of volume expansion when the temperature rises.
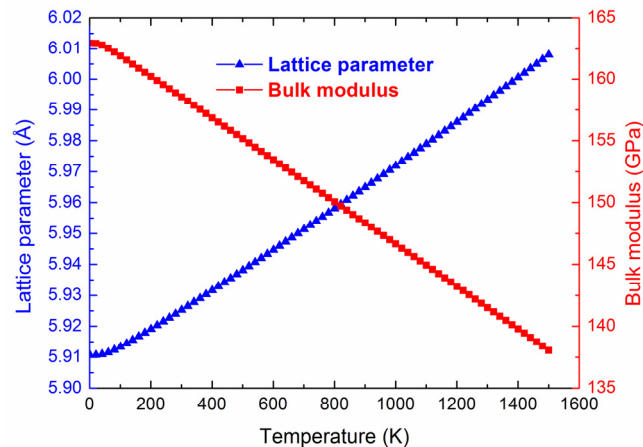
Figure 2. Temperature dependence of the lattice parameter and bulk modulus of $AlNi_2Ti$.

In addition, the compressibility calculated from the ratio of volume (V) under a certain pressure to original volume (V_0) without pressing is adopted to characterize the stability under high pressure and plasticity. Figure 3 shows the computed results of $AlNi_2Ti$ as well as some ceramic and metal materials for comparison. From Figure 3, under the same pressure, the volume change of $AlNi_2Ti$ is larger than TiO, TiO_2, Fe, α-Al_2O_3 and diamond, so the intermetallic compound $AlNi_2Ti$ performs the best plasticity and deformation ability.
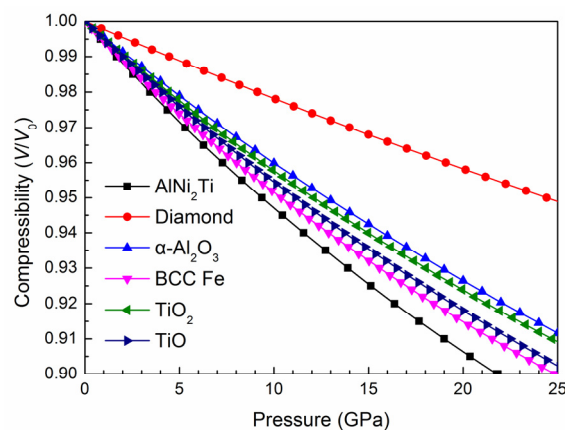
Figure 3. Compressibility characterized by normalized volume versus pressure of $AlNi_2Ti$, as well as diamond, α-Al_2O_3, BCC-iron, TiO_2 and TiO for comparison.

3.2. Anisotropy of Mechanical Moduli

The elastic anisotropy of AlNi$_2$Ti with cubic structure is investigated by computing the values of bulk and Young's moduli under different directions, as in the following equations [75]:

$$B = 1/(s_{11} + 2s_{12}), \tag{5}$$

$$E = 1/\left[s_{11} - 2\left(s_{11} - s_{12} - \frac{1}{2}s_{44} \right)\left(l_1^2 l_2^2 + l_2^2 l_3^2 + l_3^2 l_1^2 \right) \right], \tag{6}$$

Here s_{ij} represents the elastic compliance matrix, which is the inverse matrix of c_{ij}. l_1, l_2 and l_3 are the directional cosines. In spherical coordinates, l_1, l_2 and l_3 are computed by $l_1 = \sin\theta\cos\varphi$, $l_2 = \sin\theta\sin\varphi$, and $l_3 = \cos\theta$ respectively. Then the obtained three-dimensional contour plots of elastic moduli are shown in Figure 4, revealing that the bulk modulus of AlNi$_2$Ti shows spherical morphology while the Young's modulus shows relatively stronger anisotropy. From the planar projections of bulk and Young's moduli on [001] and [110] crystallographic planes in Figure 4, the anisotropy of the Young's modulus on both [001] and [110] planes is apparent. The bulk and Young's moduli on principal crystallographic directions can be calculated by

$$B_{[100]} = 1/(s_{11} + s_{12} + s_{13}),\ B_{[010]} = 1/(s_{12} + s_{22} + s_{23}),\ B_{[001]} = 1/(s_{13} + s_{23} + s_{33}), \tag{7}$$

$$E_{[100]} = 1/s_{11},\ E_{[010]} = 1/s_{22},\ E_{[001]} = 1/s_{33}, \tag{8}$$
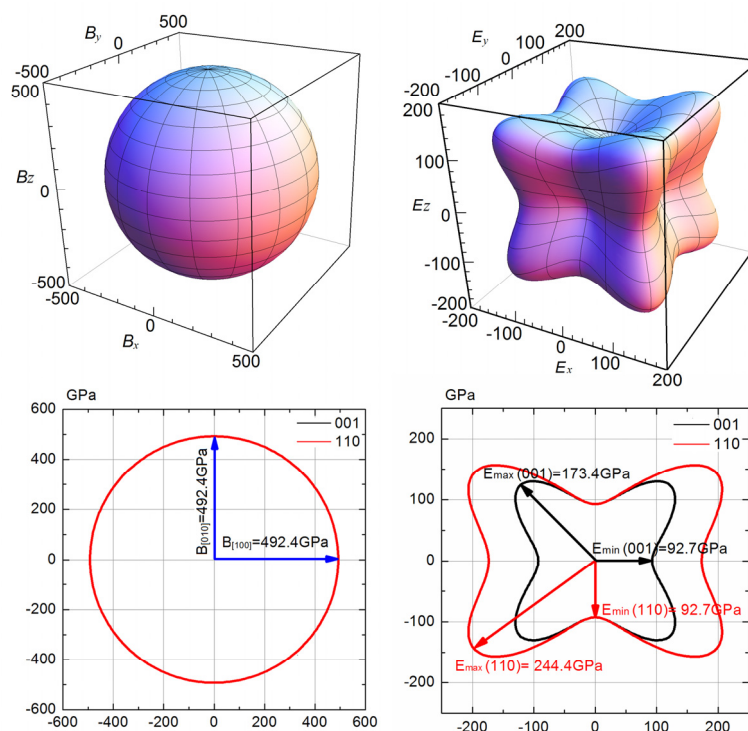
Figure 4. The surface constructions of the bulk modulus B and Young's modulus E of AlNi$_2$Ti; the corresponding planar projections of B on the [001] crystallographic plane and planar projections of E on [001] and [110] crystallographic planes are shown below.

The results indicate that the bulk modulus of AlNi2Ti is $B_{[100]} = B_{[010]} = 492.4$ GPa, which shows obvious isotropy. As for the Young's modulus, the maximum and minimum values on the [001] plane are $E_{[110]} = 173.4$ GPa and $E_{[100]} = 92.7$ GPa; the maximum and minimum values on the [110] plane are $E_{[111]} = 244.4$ GPa and $E_{[001]} = 92.7$ GPa, respectively.

Three shear anisotropic factors (A_1, A_2 and A_3) for cubic crystal are calculated to characterize the elastic anisotropy, which were defined by Ravindran et al. as $A_1 = A_2 = A_3 = 2c_{44}/(c_{11} - c_{12})$ [76]. As in Table 2, the computed values of A_1, A_2 and A_3 were 2.96 by the GGA-PBE method and 2.88 by the GGA-PW91 method, demonstrating that the shear modulus of AlNi$_2$Ti has a strong directional dependence, because the values of A_1, A_2 and A_3 should be one for an isotropic crystal [77]. Besides, Ranganathan and Ostoja-Starzewski proposed another universal anisotropy index A^U determined by [78]:

$$A^U = 5(G_V/G_R) + (B_V/B_R) - 6, \tag{9}$$

The elastic anisotropy can also be evaluated by the percent anisotropies A_B and A_G in compression and shear modes as follows [79]:

$$A_B = (B_V - B_R)/(B_V + B_R), \tag{10}$$

$$A_G = (G_V - G_R)/(G_V + G_R), \tag{11}$$

The results in Table 2 show that our results are close to the data calculated by others. The value of A^U over zero implies that AlNi$_2$Ti shows the universal anisotropy of mechanical moduli; A_B has zero value while the value of A_G is slightly larger than zero, so AlNi$_2$Ti has isotropic bulk modulus and anisotropic shear modulus [77], which agrees well with the results from the Voigt and Reuss approximations.

3.3. Sound Velocities and Thermal Conductivity

The sound velocity in a crystal is an important parameter for thermodynamic properties. For cubic structure, the sound velocities of both longitudinal and transverse waves on principal crystallographic directions should be evaluated by the procedure of Braggar using elastic constants, as in the relations below [80–83]:

$$\text{for } [100]v_l = \sqrt{c_{11}/\rho}, [010]v_{t1} = [001]v_{t2} = \sqrt{c_{44}/\rho}, \tag{12}$$

$$\text{for } [110]v_l = \sqrt{(c_{11} + c_{12} + 2c_{44})/2\rho}, [1\bar{1}0]v_{t1} = \sqrt{(c_{11} - c_{12})/\rho}, [001]v_{t2} = \sqrt{c_{44}/\rho}, \tag{13}$$

$$\text{for } [111]v_l = \sqrt{(c_{11} + 2c_{12} + 4c_{44})/3\rho}, [11\bar{2}]v_{t1} = v_{t2} = \sqrt{(c_{11} - c_{12} + c_{44})/3\rho}, \tag{14}$$

Here ρ is the theoretical density of the compound; v_l is the longitudinal sound velocity; v_{t1} and v_{t2} are the first and the second transverse mode, respectively. Obviously, c_{11} determines the longitudinal sound velocity along [100] direction, while c_{44} corresponds to the transverse modes. The sound velocities in the [110] and [111] directions are related to all values of c_{11}, c_{12} and c_{44}. The anisotropy of sound velocities implies the elastic anisotropy of crystal. The calculated results are tabulated in Table 3. For comparison, the sound velocities of the Ni$_3$Ti intermetallic compound with a hexagonal structure are also calculated. It is indicated that the longitudinal sound velocities along all directions of Ni$_3$Ti are higher than AlNi$_2$Ti.

Table 3. Calculated anisotropic sound velocities of AlNi$_2$Ti intermetallic compounds, together with the values of Ni$_3$Ti. The unit of velocity is m/s.

Species	[100]			[010]			[001]			[110]			[111]			v_l	v_t	v_m
	v_l	v_{t1}	v_{t2}	v_l	v_{t1}	v_{t2}	v_l	v_{t1}	v_{t2}	v_l	v_{t1}	v_{t2}	v_l	v_{t1}	v_{t2}			
AlNi$_2$Ti	5797	3971	3971	5797	3971	3971	5797	3971	3971	6637	3262	3971	6894	2967	2967	6334	3195	3583
Ni$_3$Ti	6565	3277	3625	6565	3277	3625	6565	3277	3277	6565	3277	3625	7243	1172	3513	6427	3550	3955

Besides, the total transverse, longitudinal and mean sound velocities (v_t, v_l and v_m) can be calculated from density ρ, bulk and shear moduli (B and G), as following equations [84,85].

$$v_t = \sqrt{\frac{G}{\rho}}, \tag{15}$$

$$v_l = \sqrt{\frac{\left(B + \frac{4}{3}G\right)}{\rho}}, \tag{16}$$

$$v_m = \left[\frac{1}{3}\left(\frac{2}{v_t^3} + \frac{1}{v_l^3}\right)\right]^{-1/3}, \tag{17}$$

In Table 3, the velocities of AlNi$_2$Ti are slightly lower than Ni$_3$Ti. Once the mean sound velocities are obtained, the Debye temperature (Θ_D) can be estimated by [86]:

$$\Theta_D = \frac{h}{k_B}\left[\frac{3n}{4\pi}\left(\frac{N_A\rho}{M}\right)\right]^{1/3}v_m, \tag{18}$$

where h is the Planck's constant; k_B is the Boltzmann constant; N_A is the Avagadro's constant; n is the number of atoms per formula; and M is the molecular weight. The calculated Debye temperature values of AlNi$_2$Ti and Ni$_3$Ti are shown in Table 4. Our results are in good agreement with both the theoretical values and experimental data [35,87]. The Debye temperature of Ni$_3$Ti is higher than that of AlNi$_2$Ti, so the inter-atomic force in Ni$_3$Ti is correspondingly stronger than AlNi$_2$Ti. This may be the reason why the moduli of Ni$_3$Ti are relatively larger than AlNi$_2$Ti.

Table 4. Calculated thermodynamic parameters: Debye temperatures (K), and minimum thermal conductivities (k, W/(m·K)) of the AlNi$_2$Ti intermetallic compound and Ni$_3$Ti for comparison.

Species	Model	Θ_D	$\overline{M}$ (10^{-26})	P (10^{28})	[100] k_{min}	[010] k_{min}	[001] k_{min}	[110] k_{min}	[111] k_{min}	k_{min}	k (Exp.)
AlNi$_2$Ti	Clark	455.1 (462 [a], 411 [b])	7.97		0.85	0.85	0.85	1.16	1.37	1.14	21.4 [c]
	Cahill			7.76	1.39	1.39	1.39	1.40	1.30	1.29	
Ni$_3$Ti	Clark	516.6	9.29		1.36	1.36	1.45	1.36	1.26	1.31	
	Cahill			8.43	1.44	1.44	1.40	1.44	1.28	1.45	

[a] Cal. data from [35]; [b] Exp. data from [87]; [c] Exp. data from [2].

Thermal conductivity characterizes the thermal transportation behavior of material. In this study, the minimum thermal conductivity (k_{min}) of AlNi$_2$Ti as well as Ni$_3$Ti for comparison is estimated by Clarke's model and Cahill's model as follows [88,89]:
in Clark's model,

$$k_{min} = 0.87k_B\overline{M}^{-2/3}E^{1/2}\rho^{1/6}, \tag{19}$$

in Cahill's model,

$$k_{min} = \frac{k}{2.48}P^{2/3}(v_l + 2v_t), \tag{20}$$

where k_B is the Boltzmann constant; $\overline{M} = M/(m\cdot N_A)$ represents the average mass per atom; E is the Young's modulus; ρ is the density; P is the density of number of atoms per volume; and v_l and v_t refer to the longitudinal and transverse sound velocities, respectively. The results in Table 4 show that the minimum thermal conductivities of AlNi$_2$Ti predicted by Clark's model (1.14 W·m^{-1} K^{-1}) are slightly smaller than Cahill's model (1.29 W·m^{-1} K^{-1}). The minimum thermal conductivities of AlNi$_2$Ti by both models are close to that of Ni$_3$Ti, while the values of AlNi$_2$Ti are relatively smaller, probably due to the higher modulus of Ni$_3$Ti. The calculated thermal conductivities are smaller than the experimental value [2], because the experimental measurement is conducted using AlNi$_2$Ti alloy

rather than single phase. Besides, the anisotropy of minimum thermal conductivity estimated by Clark's model is consistent with that by Cahill's model to some degree. The k_{min} has the same value in the [100], [010] and [001] directions by both models. However, the largest k_{min} estimated within Clark's model is 1.37 W·m^{-1} K^{-1} in [111] direction; as for Cahill's model, the largest k_{min} (1.40 W·m^{-1} K^{-1}) is in [110] direction.

3.4. Thermal Expansion Coefficient and Heat Capacity

The Helmholtz free energy $E(V, T)$-V curves under different temperatures are obtained and presented in Figure 5. Then the equilibrium volumes at each temperature can be computed by fitting the Birch–Murnaghan equation of state. The volume expansions (V/V_0) under various temperatures are shown in Figure 6. It can be seen that the volume expansion of AlNi$_2$Ti increases with temperature and is greater than that of Ni-Ti binary compounds, which were investigated in reference [55].
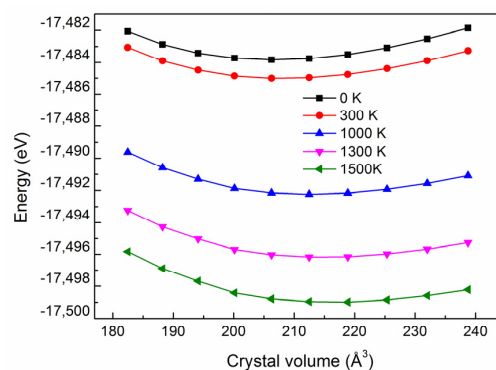
Figure 5. Dependence of the Helmholtz free energy $E(V, T)$ on the crystal volume of AlNi$_2$Ti under different temperatures.
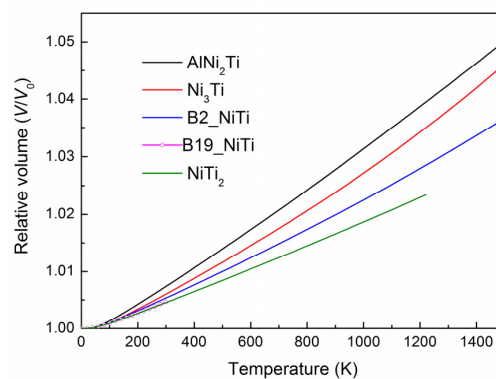
Figure 6. Volume expansions evaluated by V/V_0 as a function of temperature, where V_0 refers to the equilibrium volume at 0 K.

Then the volumetric TEC λ can be calculated by $\lambda = (\partial V/\partial T)/V$. Moreover, the linear TEC α of cubic AlNi$_2$Ti determined as $\alpha = \lambda/3$ is near the LTEC of Ni$_3$Ti, and higher than other Ni-Ti binary compounds, as shown in Figure 7. With the temperature rising, the LTEC of AlNi$_2$Ti increases rapidly first and then shows nearly linear growth with relatively slow increments above 200 K. At room temperature (300 K approximately), the LTECs of AlNi$_2$Ti and Ni-Ti binary compounds are AlNi$_2$Ti: 10.6 × 10^{-6} K^{-1}, Ni$_3$Ti: 8.92 × 10^{-6} K^{-1}, B2_NiTi: 7.50 × 10^{-6} K^{-1}, NiTi$_2$: 6.31 × 10^{-6} K^{-1}, respectively, so AlNi$_2$Ti has the largest LTEC. However, the LTEC of Ni$_3$Ti increases faster and exceeds the LTEC of AlNi$_2$Ti under elevated temperatures above 1200 K. Since AlNi$_2$Ti is considered one of the interfacial phases in ZTA-reinforced iron matrix composite, the thermal matching property of the

ZTA/Fe interface should be improved as much as possible. In this study, the LTEC of AlNi$_2$Ti is quite near to ZTA (7.0–9.5 $\times$ 10^{-6} K^{-1} [90]) and Fe (9.2–16.9 $\times$ 10^{-6} K^{-1} [91]), so the ZTA/Fe composite with AlNi$_2$Ti at the interface will have excellent thermal shock resistance.
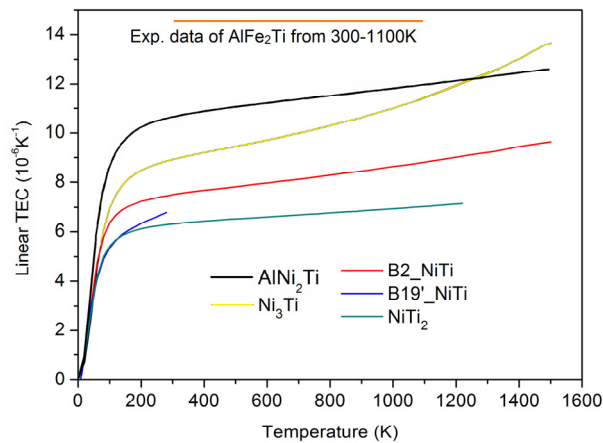
Figure 7. Linear thermal expansion coefficients of AlNi$_2$Ti and Ni-Ti binary compounds as a function of temperature [52].

Figure 7 also shows the LTEC of another Heusler compound AlFe$_2$Ti (14.5 $\times$ 10^{-6} K^{-1} [52]), which is higher than our result. In addition, the specific heats at constant pressure (C_p) and constant volume (C_v) are studied and their values follow the equation

$$C_p - C_v = \lambda^2 V(T)TB, \tag{21}$$

where λ is the volumetric thermal expansion coefficient; $V(T)$ and B are the cell volume and crystal bulk modulus at temperature T. The calculated results for specific heats are shown in Figure 8, indicating that our results agree well with the measured C_p of AlNi$_2$Ti in experiment from 102 to 606.1 K [92]. At low temperature, C_p and C_v both increase rapidly with the temperature rising and the increment speed decreases substantially at higher temperatures. The high temperature limit of C_v tends to approaching the classic Dulong–Petit limit, and C_p keeps growing due to the work done by the volumetric expansion.
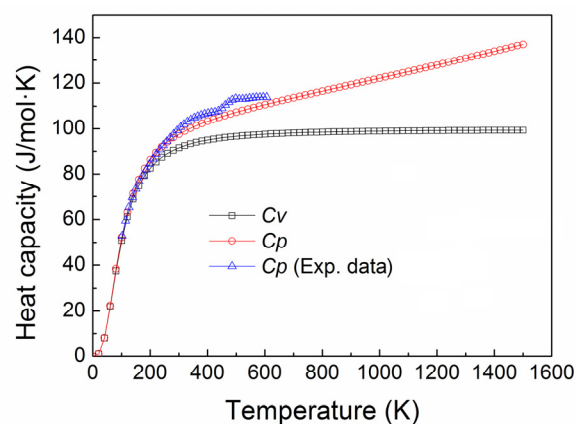
Figure 8. The specific heats at constant pressure (C_p) or volume (C_p) of AlNi$_2$Ti as a function of temperature [92].

In order to explore the low-temperature heat capacity of $AlNi_2Ti$ with metallic features, C_p can be estimated from the calculations of the electronic structures and elastic constants, which is given by [67].

$$C_p(T) = \gamma T + \beta T^3, \tag{22}$$

$$\gamma = \frac{1}{3}\pi^2 k_B^2 D_f, \tag{23}$$

$$\beta = \frac{12\pi^4 Rn}{5\Theta_D^3}, \tag{24}$$

where γ and β are the coefficients of electronic and lattice heat, respectively; D_f is the density of state (DOS) value at the Fermi level; R is the molar gas constant and n is the total number of atoms per formula unit. It is worth mentioning that Θ_D can only describe the temperature-dependence of C_p when the temperature is lower than $\Theta_D/10$ [93]. Therefore, the values of D_f, γ and β are shown in Table 5 and the C_p-T curve of $AlNi_2Ti$ and Ni-Ti binary compounds for comparison from 0 to 45 K is obtained in Figure 9.

Table 5. Theoretically calculated low-temperature specific heat of $AlNi_2Ti$ and Ni-Ti binary compounds, including the total density of states at the Fermi level (D_f, states/(eV·atom)), the characteristic parameters of electron (γ, mJ/(K^2·mol)) and phonon (β, mJ/(K^4·mol)) specific heat, and the specific heat (C_p, J/(K·mol)) at 3 K and 30 K for comparison.

Species	D_f	γ	β	C_p (3 K)	C_p (30 K)
$AlNi_2Ti$	0.416	0.981	0.0825	0.00517	2.26
Ni_3Ti	0.113	0.267	0.0569	0.00234	1.54
B2_NiTi	0.714	1.68	0.0577	0.00661	1.61
B19'_NiTi	0.406	0.957	0.0806	0.00505	2.21
$NiTi_2$	0.763	1.80	0.115	0.00850	3.16
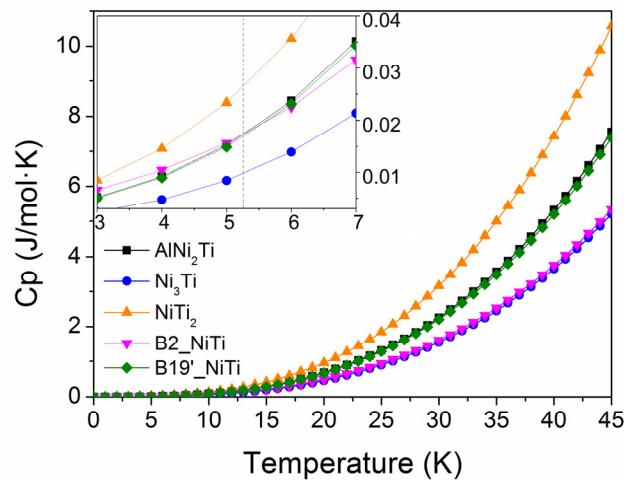
Figure 9. The heat capacity of $AlNi_2Ti$ and Ni-Ti binary compounds plotted in the range of 0–45 K.

From the illustration at the top left corner of Figure 9, it can be seen that at temperatures up to around 5.25 K, the values of C_p have the following order: $NiTi_2$ > B2_NiTi > $AlNi_2Ti \approx$ B19'_NiTi > Ni_3Ti, which is the same as the sequence of γ, indicating that the main contribution to C_p is the excitation of electrons at first. The smallest value of γ is from Ni_3Ti ($\gamma = 0.267$ mJ/(K^2·mol)), because it has the smallest DOS value at the Fermi level and thus the weakest metallic nature among these compounds. At the temperature from 5.25 to 45 K, and contributions from phonon excitations (β) have

to be taken into account, so the various growth rates result in a different order of C_p: $NiTi_2 > AlNi_2Ti$ $\approx B19'\_NiTi > B_2\_NiTi \approx Ni_3Ti$, the same sequence as β. The calculated results of C_p in Table 5 give the examples below and above 5.25 K, which can demonstrate the distinction clearly. Therefore, it is concluded that the C_p curve is dominated by the heat capacity from electrons at first and when the temperature further rises the heat capacity is mainly determined by phonon excitation.

3.5. Formatting of Mathematical Components

The electronic properties of $AlNi_2Ti$ are investigated by calculating the total density of states (TDOS) and partial density of states (PDOS). As shown in Figure 10, there are two sharp peaks which arise from the Ti-3s and 3p states respectively in the lower energy part of the DOS curve. They are localized and have little effect on chemical bonding. Around the Fermi level, the DOS is mainly composed of three wide peaks. The resonance peak I appearing in the DOS is caused by the hybridization of Al-p and Ni-d orbitals. There exists a hollow between peaks II and III, which reflects the splitting of bonding and anti-bonding states. The bonding states (peak II) mainly consists of Al-p and Ni-d states, while the anti-bonding states above the Fermi level are a conduction band composed of 3d bands of Ti, which form peak III. Obviously, the metallic nature of $AlNi_2Ti$ can be determined by a nonzero DOS value at the Fermi level (3.81 electrons/eV·f.u.), which provides this compound with an excellent ductile character.
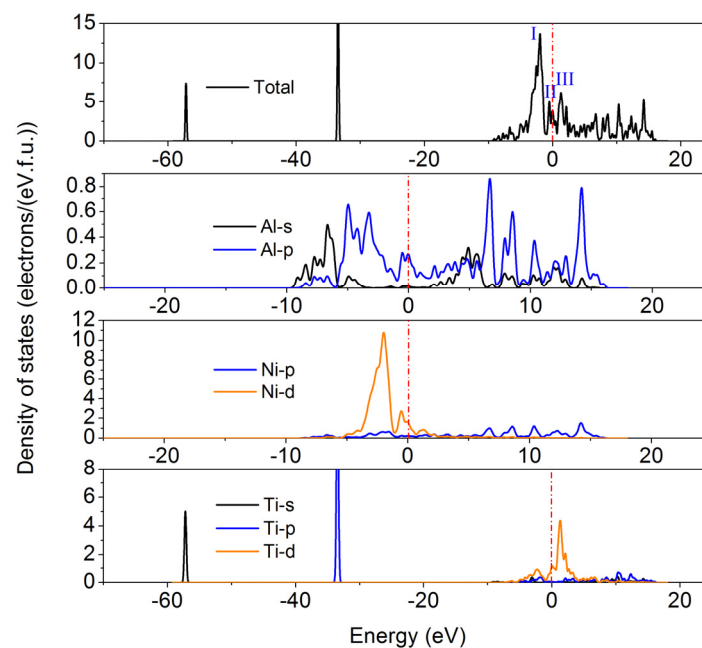
Figure 10. Total and partial density of states of $AlNi_2Ti$ compound. The Fermi level is indicated by a red vertical line.

4. Conclusions

The mechanical and thermodynamic properties of $AlNi_2Ti$ were investigated by first-principles calculations based on DFT. The mechanical moduli of $AlNi_2Ti$ were computed from the independent elastic constants. The computed values of bulk, shear and Young's modulus were 164.2, 63.2 and 168.1 GPa, respectively, indicating that it has relatively high mechanical properties. The hardness of $AlNi_2Ti$ (4.4 GPa) is comparable to common ferrous materials, like martensite steel and white cast iron. Compared with Ni-Ti binary compounds, the hardness and moduli of $AlNi_2Ti$ are much higher than $NiTi$ and $NiTi_2$, but lower than Ni_3Ti. The intrinsic ductile nature and strong metallic bonding character of $AlNi_2Ti$ are confirmed by B/G and Poisson's ratio. Besides, $AlNi_2Ti$ shows the

isotropy bulk modulus and anisotropic elasticity in different crystallographic directions. Therefore, the existence of AlNi$_2$Ti at the ZTA/Fe interface will probably benefit the mechanical properties of the composite. At room temperature, the linear thermal expansion coefficient (LTEC) of AlNi$_2$Ti, estimated by quasi-harmonic approximation based on the Debye model, was 10.6×10^{-6} K^{-1}, quite close to LTECs of ZTA and iron, so the thermal shock resistance of the ZTA/Fe composite with an AlNi$_2$Ti interfacial phase can be improved. Other thermodynamic properties including Debye temperature, sound velocity, thermal conductivity and heat capacity were also calculated and compared with Ni-Ti binary compounds. The electronic properties of AlNi$_2$Ti imply its excellent ductile character.

Author Contributions: Yefei Li conceived the total investigation and performed the calculations; Shuli Tang analyzed the data and wrote the paper; Yimin Gao supervised the whole work; Qiaoling Zheng contributed the device; Zhiwei Liu and Xiangyi Ren revised the paper.

Conflicts of Interest: The authors declare no conflict of interest. The founding sponsors had no role in the design of the study; in the collection, analyses, or interpretation of data; in the writing of the manuscript, and in the decision to publish the results.

References

1.   Heusler, F. Ueber magnetische manganlegierungen (on magnetic manganese alloys). *Verhandlungen der Deutschen Physikalischen Gesellschaft* **1903**, *5*, 219. (In German)

2.   Nakata, J.; Terada, Y.; Takizawa, S.; Ohkubo, K.; Mohri, T.; Suzuki, T. Thermal conductivity in X_2YZ heusler type intermetallic compounds. *Mater. Trans. JIM* **1996**, *37*, 442–447. [CrossRef]

3.   Oxley, D.P.; Tebble, R.S.; Williams, K.C. Heusler alloys. *J. Appl. Phys.* **1963**, *34*, 1362–1363. [CrossRef]

4.   Bradley, A.J.; Rogers, J.W. The crystal structure of the Heusler alloys. *Proc. R. Soc.* **1934**, *A144*, 340–359. [CrossRef]

5.   Wilson, A.W.; Howe, J.M. Effect of alloying additions on beta' precipitation in NiAl-Ti base alloys. *Acta Mater.* **2001**, *49*, 2653–2660. [CrossRef]

6.   Koizumi, Y.; Ro, Y.; Nakazawa, S.; Harada, H. NiTi-base intermetallic alloys strengthened by Al substitution. *Mater. Sci. Eng. A* **1997**, *223*, 36–41. [CrossRef]

7.   Lin, W.; Freeman, A.J. Cohesive properties and electronic-structure of Heusler L2$_1$-phase compounds Ni$_2$XAl (X = Ti, V, Zr, Nb, Hf and Ta). *Phys. Rev. B* **1992**, *45*, 61–68. [CrossRef]

8.   Ramos, A.S.; Vieira, M.T.; Simoes, S.; Viana, F.; Vieira, M.F. Reaction-assisted diffusion bonding of advanced materials. *Defect. Diffus. Forum* **2010**, *297–301*, 972–977. [CrossRef]

9.   Bozzolo, G.; Khalil, J.; Bartow, M.R.; Noebe, D. Atomistic modeling of ternary and quaternary ordered intermetallic alloys. In *Materials Research Society Symposium Proceedings Vol. 646, Proceedings of the High-Temperature Ordered Intermetallic Alloys IX. Symposium, Boston, MA, USA, 27–29 November 2000*; Schneibel, J.H., Hemker, K.J., Noebe, R.D., Hanada, S., Sauthoff, G., Eds.; Materials Research Society: Warrendale, PA, USA, 2001; p. N6.2.1-8.

10.   Bozzolo, G.; Noebe, R.B.; Ferrante, J. BFS simulation and experimental analysis of the effect of Ti additions on the structure of NiAl. *J. Comput. Aided Mater. Des.* **1999**, *6*, 33–68. [CrossRef]

11.   Bozzolo, G.; Noebe, R.B.; Ferrante, J.; Garg, A. Atomistic simulations of alloying additions to NiAl. *Mater. Sci. Eng. A* **1997**, *239–240*, 769–776. [CrossRef]

12.   Gale, W.F.; Abdo, Z.A.M. Microstructural development in cast alloys based on the β-NiAl–β'-Ni$_2$AlTi–γ'-Ni$_3$Al–α-Cr system. *J. Mater. Sci.* **1998**, *33*, 2299–2304. [CrossRef]

13.   Field, R.D.; Darolia, R.; Lahrman, D.F. Precipitation in NiAl/Ni$_2$AlTi alloys. *Scr. Metall.* **1989**, *23*, 1469–1474. [CrossRef]

14.   Cahn, R.W. Nickel Alumina-Titanium Alloy Contg. Epitaxially Related Phases-Having Combined Strength, High Temp. Creep Resistance and Room Temp. Ductility or Plastic Deformability, for Gas Turbine Components. Patent WO9209712-A1, 11 June 1992.

15. Matano, T.; Kimura, Y.; Miura, S.; Mishima, Y. Microstructure and mechanical properties of the L1$_2$/L2$_1$ two-phase alloys in the quaternary Co-Al-Ni-Ti system. In *High-Temperature Ordered Intermetallic Alloys VI. Symposium, Vol. 2, Proceedings of the High-Temperature Ordered Intermetallic Alloys VI. Symposium, Boston, MA, USA, 28 November–1 December 1994*; Horton, J., Baker, I., Hanada, S., Noebe, R.D., Schwartz, D.S., Eds.; Materials Research Society: Pittsburgh, PA, USA, 1995; pp. 1377–1382.

16. Mishima, Y.; Lee, E.H.; Liu, C.T. Microstructure, phase constitution and tensile properties of Co-Ni-Ti-Al base multiphase intermetallic alloys. *Mater. Trans.* **1995**, *36*, 1031–1040. [CrossRef]

17. Song, G.; Sun, Z.Q.; Poplawsky, J.D.; Xu, X.D.; Chen, M.W.; Liaw, P.K. Primary and secondary precipitates in a hierarchical-precipitate-strengthened ferritic alloy. *J. Alloys Compd.* **2017**, *706*, 584–588. [CrossRef]

18. Song, G.; Sun, Z.Q.; Li, L.; Clausen, B.; Zhang, S.Y.; Gao, Y.F.; Liaw, P.K. High temperature deformation mechanism in hierarchical and single precipitate strengthened ferritic alloys by in situ neutron diffraction studies. *Sci. Rep.* **2017**, *7*. [CrossRef] [PubMed]

19. Song, G.; Sun, Z.Q.; Clausen, B.; Liaw, P.K. Microstructural characteristics of a Ni$_2$TiAl-precipitate-strengthened ferritic alloy. *J. Alloys Compd.* **2017**, *693*, 921–928. [CrossRef]

20. Song, G.L.; Sun, Z.Q.; Poplawsky, J.D.; Gao, Y.F.; Liaw, P.K. Microstructural evolution of single Ni$_2$TiAl or hierarchical NiAl/Ni$_2$TiAl precipitates in Fe-Ni-Al-Cr-Ti ferritic alloys during thermal treatment for elevated-temperature applications. *Acta Mater.* **2017**, *127*, 1–16. [CrossRef]

21. Song, G.; Sun, Z.Q.; Li, L.; Xu, X.D.; Rawlings, M.; Liebscher, C.H.; Clausen, B.; Poplawsky, J.; Leonard, D.N.; Huang, S.Y. Ferritic alloys with extreme creep resistance via coherent hierarchical precipitates. *Sci. Rep.* **2015**, *5*. [CrossRef] [PubMed]

22. Qian, F.; Sharp, J.; Rainforth, W.M. Microstructural evolution of Mn-based maraging steels and their influences on mechanical properties. *Mater. Sci. Eng. A* **2016**, *674*, 286–298. [CrossRef]

23. Qian, F.; Sharp, J.; Rainforth, W.M. Characterisation of L2$_1$-ordered Ni$_2$TiAl precipitates in Fe-Mn maraging steel. *Mater. Charact.* **2016**, *118*, 199–205. [CrossRef]

24. Liebscher, C.H.; Radmilovic, V.R.; Dahmen, U.; Vo, N.Q.; Dunand, D.C.; Asta, M.; Ghosh, G. A hierarchical microstructure due to chemical ordering in the bcc lattice: Early stages of formation in a ferritic Fe-Al-Cr-Ni-Ti alloy. *Acta Mater.* **2015**, *92*, 220–232. [CrossRef]

25. Sun, Z.; Liebscher, C.H.; Huang, S.; Teng, Z.; Song, G.; Wang, G.; Asta, M.; Rawlings, M.; Fine, M.E.; Liaw, P.K. New design aspects of creep-resistant NiAl-strengthened ferritic alloys. *Scr. Mater.* **2013**, *68*, 384–388. [CrossRef]

26. Raqlings, M.J.S.; Liebscher, C.H.; Asta, M.; Dunand, D.C. Effect of titanium additions upon microstructure and properties of precipitation-strengthened Fe-Ni-Al-Cr ferritic alloys. *Acta Mater.* **2017**, *128*, 103–112. [CrossRef]

27. Jung, J.; Ghosh, G.; Isheim, D.G.; Olson, B. Design of nanodispersion strengthened TiNi-base shape memory alloys. In Proceedings of the International Conference on Shape Memory and Superelastic Technologies, Pacific Grove, CA, USA, 5–8 May 2003; Pelton, A.R., Duerig, T., Eds.; SMST Society Inc.: Menlo Park, CA, USA, 2004; pp. 23–32.

28. Hsu, D.H.D.; Hornbuckle, B.C.; Valderrama, B.; Barrie, F.; Henderson, H.B.; Thompson, G.B.; Manuel, M.V. The effect of aluminum additions on the thermal, microstructural, and mechanical behavior of NiTiHf shape memory alloys. *J. Alloys Compd.* **2015**, *638*, 67–76. [CrossRef]

29. Shi, J.; Gao, Z.H.; Hu, K.; Pan, G.J.; Wei, M.Z.; Xu, L.J.; Meng, X.K. High pseudoelasticity of nanoscale L2$_1$ phase-Ni43Ti38Al19 thin films. *Mater. Lett.* **2014**, *115*, 79–81. [CrossRef]

30. Peters, M.A.; Botton, G.A.; Humphreys, C.J. The precipitation of β′ Ni$_2$TiAl from Al-doped β Ni-Ti alloys. In *Institute of Physics Conference Series Vol. 147: Electron Microscopy and Analysis 1995, Proceedings of the Institute of Physics Electron Microscopy and Analysis Group Conference, Birmingham, England, 12–15 September 1995*; Cherns, D., Ed.; IOP Publishing Ltd.: Bristol, UK, 1995; pp. 451–454.

31. Jung, J.; Ghosh, G.; Isheim, D.; Olson, G.B. Precipitation of heusler phase (Ni$_2$TiAl) from B$_2$-TiNi in Ni-Ti-Al and Ni-Ti-Al-X (X = Hf, Zr) alloys. *Metall. Mater. Trans. A* **2003**, *34*, 1221–1235. [CrossRef]

32. Jung, J.; Ghosh, G.; Olson, G.B. A comparative study of precipitation behavior of Heusler phase (Ni$_2$TiAl) from B2-TiNi in Ni-Ti-Al and Ni-Ti-Al-X (X = Hf, Pd, Pt, Zr) alloys. *Acta Mater.* **2003**, *51*, 6341–6357. [CrossRef]

33. Tang, S.L.; Gao, Y.M.; Li, Y.F.; Zheng, Q.L. Preparation and interface investigation of iron matrix composite reinforced by alumina particles sintered with Ti and Ni. *Adv. Eng. Mater.* **2016**, *18*, 1913–1920. [CrossRef]

34. Tang, S.L.; Gao, Y.M.; Li, Y.F. Investigation on wear behavior of coated ZTA particles reinforced iron matrix composite. In Proceedings of the 3rd China International Congress on Composite Materials, Hangzhou, China, 21–23 October 2017. (In Chinese)

35. Wen, Z.Q.; Zhao, Y.H.; Hou, H.; Wang, B.; Han, P.D. The mechanical and thermodynamic properties of Heusler compunds Ni_2XAl (X = Sc, Ti, V) under pressure and temperature: A first-principles study. *Mater. Des.* **2017**, *114*, 398–403. [CrossRef]

36. Reddy, P.V.S.; Kanchana, V. Ab initio study of Fermi surface and dynamical properties of Ni_2XAl (X = Ti, V, Zr, Nb, Hf and Ta). *J. Alloys Compd.* **2014**, *616*, 527–534. [CrossRef]

37. Waki, S.; Yamaguchi, Y.; Mitsugi, K. Superconductivity of Ni_2NbX (X = Al, Ga and Sn). *J. Phys. Soc. Jpn.* **1985**, *54*, 1673–1676. [CrossRef]

38. Durajski, A.P. Quantitative analysis of nonadiabatic effects in dense H_3S and PH_3 superconductors. *Sci. Rep.* **2016**, *6*. [CrossRef] [PubMed]

39. Szczęśniak, D.; Zemła, T.P. On the high-pressure superconducting phase in platinum hydride. *Supercond. Sci. Technol.* **2015**, *28*, 085018. [CrossRef]

40. Sahariya, J.; Ahuja, B.L. Electronic structure of Ni_2TiAl: Theoretical aspects and Compton scattering measurement. *Physica B* **2012**, *407*, 4182–4185. [CrossRef]

41. Zhou, Y.; Chen, Y.; Feng, Y.; Yuan, H.K.; Chen, H. First-principles study on the effect of defects on the electronic and magnetic properties of the Ti_2NiAl inverse Heusler alloy. *Eur. Phys. J. B* **2014**, *87*, 290. [CrossRef]

42. Segall, M.D.; Lindan, P.J.D.; Probert, M.J.; Pickard, C.J.; Hasnip, P.J.; Clark, S.J.; Payne, M.C. First-principles simulations: Ideas, illustrations and the CASTEP code. *J. Phys. Condens. Matter* **2002**, *14*, 2717–2744. [CrossRef]

43. Mattsson, A.E.; Schultz, P.A.; Desjarlais, M.P.; Mattsson, T.R.; Leung, K. Designing meaningful density functional theory calculations in materials science—A primer. *Modell. Simul. Mater. Sci. Eng.* **2005**, *13*, R1–R31. [CrossRef]

44. Cao, L.Z.; Shen, J.; Chen, N.X. Theoretical study of the phase stability and site preference for $R_3(Fe, T)_{29}$ (R = Nd, Sm; T = V, Ti, Cr, Cu, Nb, Mo, Ag). *J. Alloys Compd.* **2002**, *336*, 18–28. [CrossRef]

45. Monkhorst, H.J.; Pack, J.D. Special points for Brillouin-zone integrations. *Phys. Rev. B* **1976**, *13*, 5188–5192. [CrossRef]

46. Perdew, J.P.; Burke, K.; Wang, Y. Generalized gradient approximation for the exchange-correlation hole of a many-electron system. *Phys. Rev. B* **1996**, *54*, 16533–16539. [CrossRef]

47. Debski, A.; Gasior, W.; Sypien, A.; Goral, A. Enthalpy of formation of intermetallic phases from Al-Ni and Al-Ni-Ti systems. *Intermetallics* **2013**, *42*, 92–98. [CrossRef]

48. Huneau, B.; Rogl, P.; Zeng, K.; Schmid-Fetzer, R.; Bohn, M.; Bauer, J. The ternary system Al-Ni-Ti Part I: Isothermal section at 900 °C; Experimental investigation and thermodynamic calculation. *Intermetallics* **1999**, *7*, 1337–1345. [CrossRef]

49. Yin, M.; Nash, P.; Chen, W.; Chen, S. Standard enthalpies of formation of selected Ni_2YZ Heusler compounds. *J. Alloys Compd.* **2016**, *660*, 258–265. [CrossRef]

50. Pearson, W.B. *Handbook of Lattice Spacings and Structures of Metals*; Pergamon: New York, NY, USA, 1967; Volume 2.

51. Jiang, D.T.; Guo, J.T.; Shi, C.X.; Lin, D.L. Microstructure and compressive properties of in situ composite (Ni-40Al-10Ti)-(0, 20%)TiC. *J. Mater. Sci. Lett.* **2000**, *19*, 115–117. [CrossRef]

52. Yan, X.L.; Grytsiv, A.; Rogl, P.; Pomjakushin, V.; Palm, M. The Heusler phase $Ti_{25}(Fe_{50-x}Ni_x)Al_{25}$ ($0 \leq x \leq 50$); structure and constitution. *J. Phase Equilib. Diffus.* **2008**, *29*, 500–508. [CrossRef]

53. Sridharan, S.; Nowotny, H.; Wayne, S.F. Investigations within the quaternary system titanium—nickel—alumina—carbon. *Monatsh. Chem.* **1983**, *114*, 127–135. [CrossRef]

54. Hu, R.X.; Nash, P.; Chen, Q. Enthalpy of formation in the Al-Ni-Ti system. *J. Phase Equilib. Diffus.* **2009**, *30*, 559–563. [CrossRef]

55. Li, Y.F.; Tang, S.L.; Gao, Y.M.; Ma, S.Q.; Zheng, Q.L.; Cheng, Y.H. Mechanical and thermodynamic properties of intermetallic compounds in the Ni-Ti system. *Int. J. Mod. Phys. B* **2017**, *31*. [CrossRef]

56. Zhao, J.J.; Winey, J.M.; Gupta, Y.M. First-principles calculations of second- and third-order elastic constants for single crystals of arbitrary symmetry. *Phys. Rev. B* **2007**, *75*. [CrossRef]

57. Patil, S.K.R.; Khare, S.V.; Tuttle, B.R.; Bording, J.K.; Kodambaka, S. Mechanical stability of possible structures of PtN investigated using first-principles calculations. *Phys. Rev. B* **2006**, *73*. [CrossRef]

58. Born, M.; Huang, K. *Dynamical Theory of Crystal Lattices*; Oxford University Press: London, UK, 1954.

59. Wu, Z.J.; Zhao, E.J.; Xiang, H.P.; Hao, X.F.; Liu, X.J.; Meng, J. Crystal structures and elastic properties of superhard IrN_2 and IrN_3 from first principles. *Phys. Rev. B* **2007**, *76*. [CrossRef]

60. Zhang, B.; Wu, L.L.; Wan, B.; Zhang, J.W.; Li, Z.H.; Gou, H.Y. Structural evolution, mechanical properties, and electronic structure of Al-Mg-Si compounds from first principles. *J. Mater. Sci.* **2015**, *50*, 6498–6509. [CrossRef]

61. Zhou, W.; Liu, L.J.; Li, B.L.; Wu, P.; Song, Q.G. Structural, elastic and electronic properties of intermetallics in the Pt-Sn system: A density functional investigation. *Comput. Mater. Sci.* **2009**, *46*, 921–931. [CrossRef]

62. Chung, D.H.; Buessem, W.R. The elastic anisotropy of crystals. *J. Appl. Phys.* **1967**, *38*, 2010–2012. [CrossRef]

63. Chung, D.H.; Buessem, W.R. The Voigt-Reuss-Hill approximation and elastic moduli of polycrystalline MgO, CaF_2, β-ZnS, ZnSe, and CdTe. *J. Appl. Phys.* **1967**, *38*, 2535–2540. [CrossRef]

64. Chung, D.H.; Buessem, W.R. The Voigt-Reuss-Hill (VRH) approximation and the elastic moduli of polycrystalline ZnO, TiO_2 (rutile), and α-Al_2O_3. *J. Appl. Phys.* **1968**, *39*, 2777–2782. [CrossRef]

65. Xiang, H.P.; Wu, Z.J. Ab initio study on the electronic, magnetic, and mechanical properties of $CaCu_3V_4O_{12}$. *Inorg. Chem.* **2008**, *47*, 2706–2709. [CrossRef] [PubMed]

66. Chen, X.Q.; Niu, H.Y.; Li, D.Z.; Li, Y.Y. Modeling hardness of polycrystalline materials and bulk metallic glasses. *Intermetallics* **2011**, *19*, 1275–1281. [CrossRef]

67. Li, Y.F.; Gao, Y.M.; Xiao, B.; Min, T.; Fan, Z.J.; Ma, S.Q.; Xu, L.L. Theoretical study on the stability, elasticity, hardness and electronic structures of W-C binary compounds. *J. Alloys Compd.* **2010**, *502*, 28–37. [CrossRef]

68. Teter, D.M. Computional alchemy: The search for new superhard materials. *MRS Bull.* **1998**, *23*, 22–27. [CrossRef]

69. Chen, K.; Zhao, L. Elastic properties, thermal expansion coefficients and electronic structures of $Ti_{0.75}X_{0.25}C$ carbides. *J. Phys. Chem. Solids* **2007**, *68*, 1805–1811. [CrossRef]

70. Šimůnek, A.; Vackář, J. Hardness of covalent and ionic crystals: First-principle calculations. *Phys. Rev. Lett.* **2006**, *96*. [CrossRef] [PubMed]

71. Pabst, W.; Tichá, G.; Gregorová, E. Effective elastic properties of alumina-zirconia composite ceramics part 3. Calculation of elastic moduli of polycrystalline alumina and zirconia from monocrystal data. *J. Ceram.-Silikáty* **2004**, *48*, 41–48.

72. Birch, F. Finite elastic strain of cubic crystals. *Phys. Rev.* **1947**, *71*, 809–824. [CrossRef]

73. Manghnani, M.H.; Fisher, E.S.; Brower, W.S., Jr. Temperature dependence of the elastic constants of single-crystal rutile. *J. Phys. Chem. Solids* **1972**, *33*, 2149–2159. [CrossRef]

74. Otero-de-da-Roza, A.; Luaña, V. GIBBS2: A new version of the quasi-harmonic model code. I. Robust treatment of the static data. *Comput. Phys. Commun.* **2011**, *182*, 1708–1720. [CrossRef]

75. Nye, J.F. *Physical Properties of Crystals*; Oxford University Press: London, UK, 1985.

76. Ravindran, P.; Fast, L.; Korzhavyi, P.A.; Johansson, B.; Wills, J.; Eriksson, O. Density functional theory for calculation of elastic properties of orthorhombic crystals: Application to $TiSi_2$. *J. Appl. Phys.* **1998**, *84*, 4891–4904. [CrossRef]

77. Xiang, H.M.; Feng, Z.H.; Zhou, Y.C. Theoretical investigations on mechanical anisotropy and intrinsic thermal conductivity of $YbAlO_3$. *J. Eur. Ceram. Soc.* **2015**, *35*, 1549–1557. [CrossRef]

78. Ranganathan, S.I.; Ostoja-Starzewski, M. Universal elastic anisotropy index. *Phys. Rev. Lett.* **2008**, *101*. [CrossRef] [PubMed]

79. Mersol, S.A.; Lynch, C.T.; Vahldiek, F.W. *Anisotropy in Single Crystal Refractory Compounds*; Plenum Press: New York, NY, USA, 1968.

80. Brugger, K. Determination of third-order elastic coefficients in crystals. *J. Appl. Phys.* **1965**, *36*, 768–773. [CrossRef]

81. Grimvall, G. *Thermophysical Properties of Materials*; Elsevier: Amsterdam, The Netherlands, 1999.

82. Feng, J.; Xiao, B.; Wan, C.L.; Qu, Z.X.; Huang, Z.C.; Chen, J.C.; Zhou, R.; Pan, W. Electronic structure, mechanical properties and thermal conductivity of $Ln_2Zr_2O_7$ (Ln = La, Pr, Nd, Sm, Eu and Gd). *Acta. Mater.* **2011**, *59*, 1742–1760. [CrossRef]

83. Chong, X.Y.; Jiang, Y.H.; Zhou, R.; Zhu, H.; Feng, J. Electronic structure, anisotropic elastic and thermal properties of the η phase Fe_6W_6C. *Comput. Mater. Sci.* **2015**, *108*, 205–211. [CrossRef]

84. Ding, Y.C.; Xiao, B. Anisotropic elasticity, sound velocity and thermal conductivity of TiO_2 polymorphs from first principles calculations. *Comput. Mater. Sci.* **2014**, *82*, 202–218. [CrossRef]

85. Anderson, O.L. A simplified method for calculating the Debye temperature from elastic constants. *J. Phys. Chem. Solids* **1963**, *24*, 909–917. [CrossRef]

86. Kittel, C. *Introduction to Solid State Physics*, 8th ed.; John Wiley & Sons, Inc.: Hoboken, NJ, USA, 2004.

87. Rocha, F.S.D.; Fraga, G.L.F.; Brandao, D.E.; Silva, C.M.D.; Gomes, A.A. Specific heat and electronic structure of Heusler compounds Ni_2TAl (T = Ti, Zr, Hf, V, Hb, Ta). *Physica B* **1999**, *269*, 154–162. [CrossRef]

88. Clarke, D.R. Materials selection guidelines for low thermal conductivity thermal barrier coatings. *Surf. Coat. Technol.* **2003**, *163*, 67–74. [CrossRef]

89. Cahill, D.G.; Watson, S.K.; Pohl, R.O. Lower limit to the thermal conductivity of disordered crystals. *Phys. Rev. B* **1992**, *46*, 6131–6140. [CrossRef]

90. Zheng, K.H.; Gao, Y.M.; Li, Y.F.; Zhao, S.M.; Wang, J. Three-body abrasive wear resistance of iron matrix composites reinforced with ceramic particles. *Proc. Inst. Mech. Eng. Part J J. Eng. Tribol.* **2014**, *228*, 3–10. [CrossRef]

91. ASM International Handbook Committee. *ASM Handbook, Vol. 1: Properties and Selection: Irons, Steels and High-Performance Alloys*; ASM International: Geauga County, OH, USA, 1993.

92. Onderka, B.; Sypien, A.; Wierzbicka-Miernik, A.; Czeppe, T.; Zabdyr, L.A. Specific heat capacities of some ternary aluminides. *J. Phase Equilib. Diffus.* **2011**, *32*, 39–41. [CrossRef]

93. Drulis, M.K.; Czopnik, A.; Drulis, H.; Spanier, J.E.; Ganguly, A.; Barsoum, M.W. On the heat capacity of Ti_3GeC_2. *Mater. Sci. Eng. B* **2005**, *119*, 159–163. [CrossRef]